Translational Oncology
www.transonc.com
Volume 4 Number 3 June 2011 pp. 126–137 126

JLK1486, a Bis 8-Hydroxyquinoline–Substituted Benzylamine, Displays Cytostatic Effects in Experimental Gliomas through MyT1 and STAT1 Activation and, to a Lesser Extent, PPARγ Activation[1,2]

Céline Bruyère*, Sébastien Madonna†, Gwendoline Van Goietsenoven*, Véronique Mathieu*, Jean Dessolin‡, Jean-Louis Kraus†, Florence Lefranc*,§ and Robert Kiss*

*Laboratoire de Toxicologie, Faculté de Pharmacie; Hôpital Erasme, Université Libre de Bruxelles, Brussels, Belgium; †Laboratoire de Chimie Biomoléculaire, Centre National de la Recherche Scientifique, IBDML-UMR-6216, Campus de Luminy, Marseille, France; ‡Institut Européen de Chimie et Biologie, Centre National de la Recherche Scientifique UMR 5248 Chimie et Biologie des Membranes et des Nano-objets, Pessac, France; §Service de Neurochirurgie, Hôpital Erasme, Université Libre de Bruxelles, Brussels, Belgium

Abstract

Gliomas account for 5% to 7% of all solid cancers in adults and up to 30% of solid cancers in children; glioblastomas are the most malignant type of glioma and often have dismal prognoses. The alkylating agent temozolomide provides the greatest chemotherapeutic benefits currently available; however, glioblastoma patients cannot be cured. Novel drugs that efficiently combat glioblastomas are therefore of great interest. We report here that JLK1486, an 8-hydroxyquinoline–substituted benzylamine, could represent a novel chemical scaffold to reach this goal. Indeed, JLK1486 mediated anticancer activity *in vivo* (through intravenous as well as oral routes of administrations) in an orthotopic xenograft model and displayed efficiency similar to that of temozolomide. The therapeutic benefits of JLK1486 seem to relate to its ability to activate various transcription factors (including Myt1, STAT1, and peroxisome proliferator–activated receptor γ) in glioma cells. These transcription factors are implicated in the control of glioma cell proliferation, and the resultant global effect of their activation by JLK1486 was cytostatic, not cytotoxic. Thus, the current study opens the door for the development of novel compounds to combat glioblastoma using 8-hydroxyquinoline benzylamine analogs.

Translational Oncology (2011) 4, 126–137

Introduction

Brain cancers account for 10% to 15% of all solid cancers in adults and up to 30% in children, with gliomas accounting for about half of all cases in adults and more than two thirds of all cases in children [1–3]. Glioblastomas, which account for approximately 50% of gliomas, are the most malignant type of glioma and are associated with dismal prognoses because of the diffuse, invasive nature of glioblastoma cells [4–7] as well as their intrinsic resistance to proapoptotic stimuli and thus to conventional radiotherapy and chemotherapy [5,7,8]. The current standard of care for glioblastoma patients includes surgery followed by radiotherapy and concomitant and subsequent (adjuvant) chemotherapy with the alkylating drug temozolomide (TMZ) [3,9]. TMZ increases glioblastoma sensitivity to radiotherapy most effectively in O^6-methylguanine-DNA methyltransferase (MGMT)–negative

Address all correspondence to: Robert Kiss, PhD, Laboratoire de Toxicologie, Faculté de Pharmacie, Université Libre de Bruxelles, CP205/1, Campus de la Plaine, Boulevard du Triomphe, 1050 Brussels, Belgium. E-mail: rkiss@ulb.ac.be

[1]Véronique Mathieu is a postdoctoral fellow, Florence Lefranc is a postdoctoral clinician fellow, and Robert Kiss is a director of research with the Fonds National de la Recherche Scientifique (Belgium). Jean Dessolin wishes to address his deepest thanks to Ligue contre le cancer (France) and Association pour la Recherche contre le Cancer (France) for their continuous support. The Centre National de la Recherche Scientifique (France) is also acknowledged for financial support.

[2]This article refers to supplementary materials, which are designated by Tables W1 to W3 and are available online at www.transonc.com.

Received 3 November 2010; Revised 24 February 2011; Accepted 2 March 2011

1944-7124/11
DOI 10.1593/tlo.10253

glioblastomas by augmenting the degree of radiation-induced double-strand DNA damage [3,10]. TMZ-induced DNA damage provokes sustained proautophagic defenses in glioblastoma cells [11,12], a feature that ends by late apoptosis [13]. TMZ also displays antiangiogenic effects in experimental gliomas [14]. However, glioblastoma patients benefit from TMZ treatment only for a limited period because glioblastomas develop resistance to TMZ during treatment [3]. Epigenetic inactivation of the DNA repair enzyme MGMT seems to be the strongest predictive marker for outcome in TMZ-treated glioblastoma patients because MGMT can repair methyl-guanosine by demethylating guanosine, thereby allowing for double-strand break repair [15]. Prolonged treatments of experimental gliomas with an astrocytic origin leads to the emergence of certain levels of resistance to TMZ through increased expression of GLUT transporters and AKR1C proteins [16], a feature not observed in experimental gliomas with an oligodendroglial origin [17]. In addition, TMZ treatment must usually be discontinued after 12 to 18 cycles, even in responsive glioblastoma patients, because of progressive hematologic complications [3,18].

Unfortunately, clinical trials using targeted therapies against various receptors or key elements in various signaling pathways have had minimal success in treating glioblastoma patients [19,20]. It is thus of great interest to discover and develop novel chemicals aiming to combat glioblastomas that display intrinsic resistance to apoptosis and/or escape TMZ therapy during treatment.

The present study characterizes the anticancer activity of JLK1486, a bis 8-hydroxyquinoline–substituted benzylamine, in various *in vitro* and *in vivo* human glioma models. JLK1486 was selected from a series of 26 compounds for which we previously showed *in vitro* anticancer activity [21]. It is well known that several anticancer drugs used to treat cancer patients (cisplatin, psoralens, mitomycin C) induce interstrand DNA cross-links, and part of this mechanism of action occurs through the generation of quinone methides [22]. The compound under study, JLK1486 (Figure 1*A*), could mediate its anticancer activity, at least *in vitro*, through quinone methide intermediates, which do not react with DNA, but which yield covalent protein thiol adducts [21]. Whereas quinone methide derivatives have

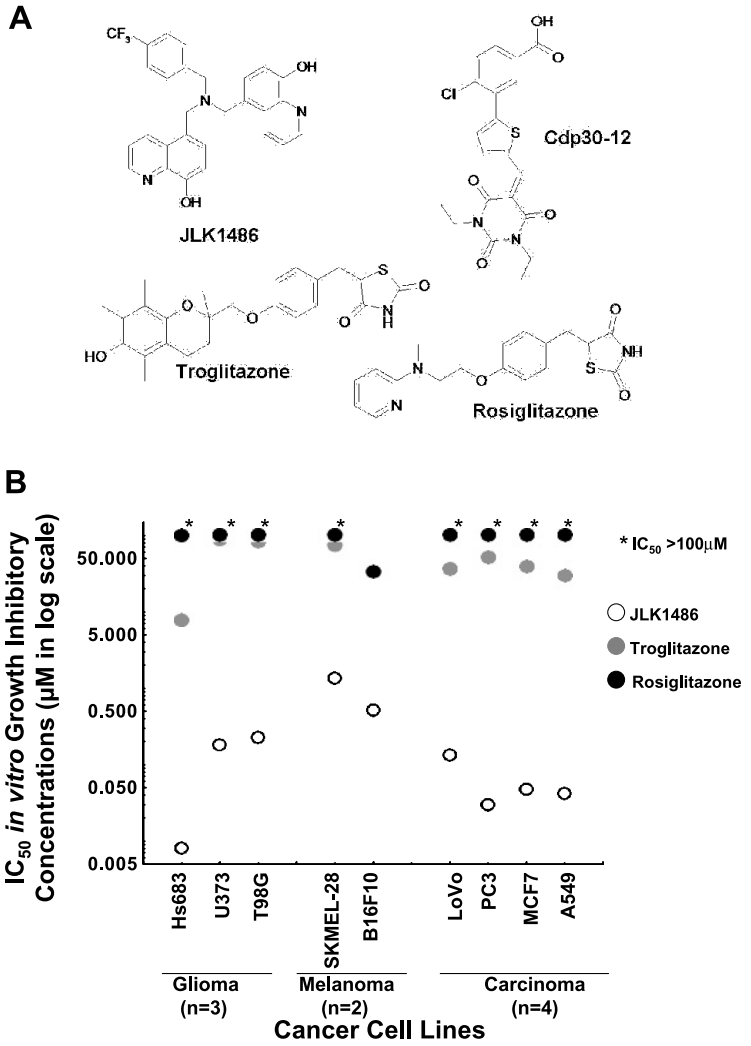

Figure 1. IC_{50} *in vitro* growth-inhibitory concentrations of JLK1486, troglitazone and rosiglitazone in nine cancer cell lines. (A) Chemical structures of JLK1486 and Cpd30-12, a STAT1 agonist, and of troglitazone and rosiglitazone, two PPARγ agonists. (B) Determination of the growth-inhibitory effects induced by JLK1486, rosiglitazone and troglitazone in nine cancer cell lines (eight human and one mouse (B16F10)), including three glioma, two melanoma, and four carcinoma models. Data are presented as mean IC_{50} values with open, gray, and black dots corresponding to JLK1486, troglitazone, and rosiglitazone, respectively. Except for B16F10 cell line, the IC_{50} values obtained for rosiglitazone were higher than 100 μM. IC_{50} values were obtained from sextuplicate for each experimental condition.

been widely studied in various types of cancers [22], our previous report [21] seems to be the first in the glioma field. Microarray analysis further showed that JLK1486 induced the expression of a variety of stress-related genes responsible for cytotoxic effects in carcinoma cells, although these genes produced cytostatic effects in glioma cells [21]. The present study, therefore, focuses on the antiglioma effects of JLK1486 *in vitro* and *in vivo* in various glioma models that display either intrinsic sensitivity or resistance to proapoptotic stimuli. We used the highly malignant, but apoptosis-sensitive, Hs683 oligodendroglioma model [17,23,24] as opposed to the highly malignant and apoptosis-resistant U373 and T98G astroglioma models [23,25,26].

Materials and Methods

Reagents

Reagents were obtained as follows: TMZ was purchased from Schering Plough (Brussels, Belgium); troglitazone and rosiglitazone were from Cayman Chemical (SpiBio, France); cell culture medium (RPMI), fetal calf serum, glutamine, gentamicin, and penicillin-streptomycin were from Invitrogen (Merelbeke, Belgium). JLK1486 was synthesized in our laboratory (J.L. Kraus) as detailed elsewhere [21].

Cell Cultures

We used one mouse and eight human cancer cell lines that were obtained from the European Collection of Cell Culture (Salisbury, UK), the American Type Culture Collection (ATCC, Manassas, VA), and the Deutsche Sammlung von Mikroorganismen und Zellkulturen (DSMZ, Braunschweig, Germany). The human cancer cell lines included the A549 non–small cell lung cancer (DSMZ code ACC107), the SKMEL-28 melanoma (ATCC code HTB-72), the Hs683 oligodendroglioma (ATCC code HTB-138), the U373 (ATCC code HTB-17), and T98G (ATCC code CRL-1690) glioblastoma, and the LoVo colon (ATCC code CCL-229), the PC3 prostate (ATCC code CRL-1435), and the MCF7 breast (ATCC code HTB-22) cancer cell lines, whereas the mouse cancer cell line was the B16F10 melanoma line (ATCC code CRL-6475). The cancer cell lines under study were cultured in RPMI medium supplemented with 10% heat-inactivated fetal calf serum, 4 mM glutamine, 100 μg/ml gentamicin, and penicillin-streptomycin (200 U/ml and 200 μg/ml).

Determination of Inhibitory Concentration 50% (IC_{50}) In Vitro *Growth-Inhibitory Concentrations*

The overall growth level of human cancer cell lines was determined using the colorimetric 3-[4,5-dimethylthiazol-2yl])-diphenyl tetrazolium bromide (Sigma, Bornem, Belgium) assay as detailed and validated previously [17,26,27]. The solvent used was DMSO (highest concentration 0.1%). Spectrophotometric analyses were performed with a Biorad Model 680XR (Biorad, Nazareth, Belgium) apparatus at 570 nm (with a reference of 630 nm). Each experimental condition was carried out in sextuplicate. Cells were used during five passages and came from liquid nitrogen tanks. After five passages, cells were eliminated, and new cell vials were used. Cell were passaged when they reached 70% to 80% confluence.

Computer-Assisted Phase-Contrast Microscopy (Quantitative Videomicroscopy)

Direct visualization of JLK1486-induced effects on Hs683 oligodendroglioma morphology was carried out using computer-assisted phase-contrast microscopy, that is, quantitative videomicroscopy, as detailed and validated previously [17,26,27]. Hs683 cancer cells were monitored for 72 hours in the absence (control) or presence of 100 nM JLK1486 (i.e., the IC_{50} growth-inhibitory concentration as calculated by 3-[4,5-dimethylthiazol-2yl])-diphenyl tetrazolium bromide assay). Movies were built using the obtained time-lapse image sequences and enabled detailed screening for cell viability to determine whether the compound under study induced cytostatic *versus* cytotoxic effects. All experimental conditions were performed in triplicate.

Determination of Cell Cycle Kinetics

The cell cycle kinetics of Hs683, T98G, and U373 glioma cells left untreated or incubated with 100 nM JLK1486 were determined by flow cytometry analysis using the terminal deoxynucleotidyl transferase deoxyuridine triphosphate nick-end labeling technique based on a previously detailed experimental protocol [28]. Each sample was evaluated in triplicate. Flow cytometry was performed using a Cell Lab Quanta flow cytometer (Beckman Coulter Analis, Suarlée, Belgium).

Determination of Mitotic Rates

Cells undergoing division exhibit very bright patterns compared with nondividing cells. On the basis of this observation, we developed a custom division detector capable of identifying cells undergoing division in time-lapse sequences [29]. This detection method is based on an automatic event detection completed by an interactive validation/correction procedure as described previously [29]. The total number of mitoses was determined in Hs683, T98G, and U373 glioma cells treated for 72 hours with 100 nM JLK1486. Each sample was evaluated in triplicate.

Determination of Apoptotic Death Features

Apoptotic rates of Hs683, T98G, and U373 glioma cells left untreated (control) or treated for 72 hours with 100 nM JLK1486 were determined using flow cytometry (terminal deoxynucleotidyl transferase deoxyuridine triphosphate nick-end labeling technique) as detailed previously [28]. Briefly, glioma cells (both nonadherent cells and adherent cells) were harvested, pooled, and fixed with 1% paraformaldehyde (for 1 hour) and overnight with 70% ethanol (for 15 hours). Then, the cells were processed using the APO-Direct Kit (BD Pharmingen, Erembodegem, Belgium) according to the manufacturer's instructions. Fluorescence intensity was analyzed immediately on a Cell Lab Quanta flow cytometer (Beckman Coulter Analis). Treatment of human PC3 prostate cancer cells with 1 μM narciclasine for 72 hours was used as a positive control.

Kinase Activity Determination

We originally prepared ProQinase (Freiburg, Germany) with JLK1486 as a stock solution in 100% DMSO, and aliquots were further diluted with water in 96-well microliter plates immediately before use. For each kinase assay, 5 μl from a 2×10^5 M/10% DMSO compound solution were transferred into the assay plates. The final volume of the assay was 50 μl. The final assay concentration of JLK1486 was 100 nM. A radiometric protein kinase assay (^{33}PanQinase Activity Assay; Table W1) was used to measure the kinase activity of the 256 protein kinases under study as detailed previously [30].

Transcription Factor Array

Hs683 cells were treated with 100 nM JLK1486. After 12 hours, cells were scraped into cold PBS buffer, and nuclear extracts were isolated from these cells using the nuclear extraction kit from Active Motif (catalog number no. 40010; Rixensart, Belgium). Arrays were performed using TranSignal protein/DNA arrays (SA Biosciences [Tebu-Bio], Boechout, Belgium) according to the manufacturer's instructions. In brief, biotin-labeled DNA binding oligonucleotides (TranSignal probe mix; Panomics [Ozyme; Montigny-Le-Bretonneau, France]) were incubated with 15 μg of nuclear extract to allow the formation of protein/DNA (or TF/DNA) complexes. The protein/DNA complexes were then separated from the free probes using the provided spin columns. The eluted and labeled probes were hybridized to the TranSignal Array membrane overnight at 42°C. Each membrane was then incubated with streptavidin–horseradish peroxidase conjugate, developed with a substrate solution containing luminol enhancer and peroxide solution, and then exposed using Hyperfilm ECL (GE Healthcare, Diegem, Belgium). Scanned films were analyzed using an Aida image analyzer (RayTest, Straubenhardt, Germany).

Peroxisome Proliferator–Activated Receptor Activation Assay

U373 cells were treated with 100 nM JLK1486 for 4 or 24 hours. After these incubations, cells were collected and nuclear extracts were purified according to the manufacturer's instructions (PPARα, PPARβ/δ, PPARγ; Complete Transcription Factor Assay Kit; Cayman Chemical). In brief, cells were detached with trypsin and centrifuged at 300*g* for 5 minutes. The pellets were resuspended in an ice-cold PBS/phosphatase inhibitor solution for 5 minutes. This step was repeated once. Extracts were resuspended in ice-cold hypotonic buffer and incubated for 15 minutes. To break the cytoplasmic membrane, cells were treated with Nonidet P40 (Sigma-Aldrich). The extracts were centrifuged and the cytoplasmic fraction was saved for other applications. The pellet was resuspended in an extraction buffer containing protease inhibitor and incubated with gentle rocking for 30 minutes on ice. Extracts were centrifuged at 14,000*g* for 10 minutes at 4°C. The supernatant contained the nuclear fraction. Nuclear extracts were loaded in 96-well plates and incubated overnight at 4°C. The primary antibody (from the PPARα, β/δ, γ; Complete Transcription Factor Assay Kit) was added and incubated for 1 hour at room temperature. The wells were washed five times, and a goat antirabbit HRP-conjugated secondary antibody was added and incubated for 1 hour at room temperature. The wells were washed five times. Developing solution was added for 45 minutes, and absorbance was measured at 450 nm with a spectrophotometer (Biorad Model 680XR; Biorad).

$p21^{waf/cip1}$ and STAT1 Activation Assay

Western blot analyses were performed as detailed previously [14,28,31]. Equal loading was verified by the bright Ponceau red coloration of the membranes, and the integrity and quantity of the extracts were assessed by tubulin immunoblot analysis. Approximately 20 μg of extracted proteins (evaluated by the bicinchoninic acid protein assay; Pierce, Perbio Science, Erembodegem, Belgium) was then loaded onto a denaturing polyacrylamide gel. The following primary antibodies were used for Western blot analysis: anti-p21 (dilution 1:200; BD Pharmingen), anti-STAT1 (dilution 1:500; BD Pharmingen), anti–phospho-STAT1 Y701 (dilution 1:250; BD Pharmingen), and antitubulin (dilution 1:3000; Abcam, Cambridge, UK). Secondary antibodies were purchased from Pierce (PerbioScience). Western blots were developed using the Pierce SuperSignal Chemiluminescence System.

Molecular Docking for Peroxisome Proliferator–Activated Receptors

Receptor and ligand preparation. Peroxisome proliferator–activated receptor α, β/δ, and γ protein coordinates were obtained from the RCSB Protein Data Bank, codes 1K7L, 1GWX, and 2PRG respectively. Three-dimensional structures were visualized and modified with Discovery Studio 2.1 (Accelrys, San Diego, CA) as follows. If dimers were present, both chains were separated and considered individually. Water molecules and protein fragments used for crystallization were removed (if any), incomplete residues were modified with the "Clean Protein" command from the Protein Reports and Utilities module, hydrogen atoms were added, and the resulting structures were saved in the pdb format. PPARγ, which was cocrystallized with rosiglitazone, was used as template to identify the binding pocket for docking experiments. The software used in this study was Vina [32], which allows side chain flexibility within the receptor during the docking process. All receptor residues within a 9-Å distance from the ligand were selected and defined as flexible. The corresponding amino acids in PPARα and PPARβ/δ were similarly chosen to allow flexibility and define the docking binding site. The receptor files for Vina experiments were prepared with AutoDock Tools [33] and utilities, where only polar hydrogen atoms were conserved in the resulting files that were saved in the pdbqt format. This file format differs from the pdb one by the presence of atomic charges that are irrelevant with any scoring function used in this study, thus no specific adjustments were necessary besides an overall control of the receptor structures. The ligands were prepared in the pdb format with DS 2.1, and ADT scripts were used to obtain the corresponding pdbqt files. All ligands were considered flexible during the docking process.

Selectivity screening. Simulations were first performed with rosiglitazone and PPARγ to check the validity of the parameters, but the obtained docked poses did not correspond to the crystals. Reduction in the number of flexible residues did not lead to any improvement in the poses, and convergence over several experiments was never attained. Finally, rosiglitazone was flexibly docked into rigid PPARγ within a 22.0 × 22.0 × 24.0 Å box centered on the ligand. In this case, the obtained poses were both consistent with the crystal structure and were convergent over five independent experiments. These parameters were then applied to the PPARα and β/δ receptors, and convergence was also observed in these cases. Troglitazone and JLK1486 were docked into the three PPARs in five independent experiments to compare their respective affinity for the different isoforms. The resulting binding energy for each compound refers to the mean calculated from the best poses. In each case, the best ligand poses were identical from one experiment to another, which constitutes the above-mentioned convergence.

Molecular Docking for STAT1 versus STAT3

Receptor and ligand preparation. STAT1 and STAT3 protein coordinates were obtained from the RCSB Protein Data Bank, codes 1BF5 and 1BG1, respectively. Three-dimensional structures were visualized and modified according to the procedure described for PPAR, but in this case, the DNA oligomers were removed. Because

the SH2 domain was the intended target, we selected the amide bond between V631 and G632 as the center of the binding pocket for docking experiments with STAT1, which correspond to the bond between V637 and G638 in STAT3. To get a wide binding site, residues within a 9-Å distance of V631-E632 were selected as flexible for STAT1, and the corresponding residues within STAT3 were deduced from the sequence alignment, which resulted in 59 and 58 torsions for the respective docking sites. To ensure a correct docking process, the search space was defined to encompass all flexible residues as a box with dimensions of 27.0 × 23.3 × 24.9 Å. Vina requires two receptor files when performing flexible docking: one corresponding to the rigid body of the protein and a second corresponding to the side chains of the previously selected residues. These files were prepared with AutoDock Tools (ADT) [33]. The ligand files were prepared in a similar manner as described for PPAR docking.

Selectivity screening. We used Cpd30-12 (Figure 1*A*), which is selective for STAT1 *versus* STAT3 [34], to verify the ability of JLK1486 to bind STAT1 rather than STAT3. Both putative ligands were docked into the previously defined active sites in five independent experiments. The resulting binding energy for each compound refers to the mean calculated from the best poses. In each case, the best ligand poses were identical from one experiment to another; the obtained energy differed because of the receptor torsion.

In Vivo *Orthotopic Hs683 Xenografting Procedures*

Hs683 glioma cells were grafted orthotopically into the brains of immunocompromised mice as described previously [17,23,24]. In each experiment, all mice (8-week-old female *nu/nu* mice; 21-23 g; Iffa Credo, Charles Rivers, Arbresle, France) had 100,000 Hs683 cells implanted on the same day into the left temporal lobe. Mice were then treated or not (control) with TMZ (40 mg/kg intravenously [i.v.] *vs* 80 mg/kg *per os*) and JLK1486 (10 mg/kg i.v. *vs* 20 mg/kg *per os*) three times per week for 3 weeks starting at day 5 after graft. *In vivo* tolerance of TMZ and JLK1486 was defined as the maximal tolerated dose, which represents the highest single dose of the compound that can be administered i.v. or orally to experimental groups of healthy mice during a maximum period of 28 days without causing death. These doses were 80 mg/kg i.v. and greater than 160 mg/kg *per os* for TMZ and 20 mg/kg i.v. and 40 mg/kg *per os* for JLK1486. We assayed each compound in each route of administration at its maximal tolerated dose/2 concentration because we administered the compounds nine times to Hs683 xenograft-bearing mice. Each experimental group contained 11 mice. Each compound has been diluted in saline (NaCl 0.9%) as a solvent and 200 μl has been administered to the mice. All *in vivo* experiments described in the present study were performed under authorization no. LA1230509 of the Animal Ethics Committee of the Federal Department of Health, Nutritional Safety, and the Environment (Belgium).

Statistics

Survival analyses were carried out by means of Kaplan-Meier curves (Statistica software; Statsoft, Tulsa, OK).

Results

IC_{50} In Vitro *Growth-Inhibitory Concentrations*

Figure 1*B* details the IC_{50} *in vitro* growth-inhibitory concentrations of JLK1486 in eight human and one mouse cancer cell lines. JLK1486 displays similar growth-inhibitory effects in glioma (Hs683, U373, T98G), melanoma (SKMEL28, B16F10), and carcinoma (LoVo, PC3, MCF7, and A549) cell lines, as well as in cancer cell lines that display actual sensitivity to proapoptotic stimuli (Hs683, B16F10, LoVo, PC3, and MCF7) and cancer cell lines that display various levels of intrinsic resistance to proapoptotic stimuli (U373, T98G, SKMEL28, and A549). The levels of apoptosis sensitivity of all these cancer cell lines have been determined in a previous work performed by our group (data not shown).

Part of the anticancer properties of JLK1486 could relate to PPARγ activation as detailed below. We, therefore, decided to compare JLK1486-induced growth-inhibitory effects *in vitro* to those associated with PPAR agonists, including troglitazone and rosiglitazone, whose chemical structures are shown in Figure 1*A*. The data in Figure 1*B* clearly indicate that JLK1486 displays higher growth-inhibitory effects than troglitazone and rosiglitazone in the nine cancer cell lines under study. These data thus suggest that PPARγ activation is not the sole mechanism by which JLK1486 exerts its antiglioma effects.

JLK1486 Induces Cytostatic, Not Cytotoxic, Effects in Glioma Cells

Quantitative videomicroscopy analysis showed that 100 nM JLK1486 impaired Hs683 cell proliferation while inducing no cytotoxic effects (Figure 2). We then decided to determine in which part of the cell cycle JLK1486 might exert its cytostatic effects in glioma cells. The IC_{50} growth-inhibitory concentration for JLK1486 was ~80 nM in Hs683, ~290 nM in T98G, and ~180 nM in U373 glioma cell lines (Figure 1*B*). We used the same concentration (i.e., 100 nM) to analyze the cytostatic effects of JLK1486 in the three glioma cell lines under study. We first investigated whether 100 nM JLK1486 induced proapoptotic, thus cytotoxic, effects in Hs683, T98G, and U373 glioma cells. Figure 3*A* shows that JLK1486 did not induce such proapoptotic effects, whereas narciclasine, the positive control in PC3 prostate cancer cells, did it. Thus, flow cytometry– (Figure 3*A*) and quantitative videomicroscopy– (Figure 2) related data perfectly fit together with respect to the fact that JLK1486 exerts its *in vitro* growth-inhibitory activity through cytostatic, not cytotoxic, effects. Flow cytometry analyses failed in revealing JLK1486-induced modifications at 100 nM in Hs683, T98G, and U373 cell cycle kinetics (Figure 3*B*). However, compound-induced effects on mitosis are rather difficult to detect by means of flow cytometry. We thus used quantitative videomicroscopy to analyze JLK1486-induced effects on the percentages of glioma cells in the mitotic phase. Figure 3*C* illustrates the morphology of mitoses whose percentages have been quantified (see Materials and Methods) in control and JLK1486-treated conditions. Figure 3*D* clearly indicates that 100 nM JLK1486 decreased mitotic rates in the three glioma cell lines under study. Altogether, data in Figures 2 and 3 point to mitosis as an important target of JLK1486-induced cytostatic effects in glioma cells.

JLK1486-Induced Cytostatic Activity in Glioma Cells Does Not Seem to Relate to Kinase Activity Inhibition

The fact that JLK1486 markedly impairs glioma cell proliferation (Figures 2 and 3, *A* and *B*) without apparent cytotoxic effects (Figures 2 and 3, *C* and *D*) prompted us to investigate whether JLK1486 might impair the activity of kinases involved either in cell cycle control or, more precisely, in mitosis control. Data from the present

study revealed that 100 nM JLK1486 did not decrease by 50% the activity of any kinase of a panel of 256 kinases that were assayed (Table W2). Whereas the human kinome includes roughly double the number of kinases as the array assayed here, the current data suggest that it is unlikely that JLK1486 impairs glioma cell proliferation through the targeting of kinases implicated in cell cycle and/or mitosis control.

JLK1486 Transiently Activates PPARγ

We made use of a Transcription Factor Array to investigate whether JLK1486 could target certain transcription factors implicated in cell proliferation (Table 1). Indeed, data in Table 1 show that 100 nM JLK1486 increased the activity of a dozen transcription factors whose activity directly regulate cell proliferation by two- to fivefold, with most of them targeting mitosis. We made use of biochemical analyses to validate, at least partly, the data provided in Table 1. Data in Figure 4 show that 100 nM JLK1486 transiently activated PPARγ while having weak or no effects on PPARα and PPARβ/δ.

Docking experiments confirmed that JLK1486 possesses a theoretical binding affinity for PPARs, including PPARγ, similar to that displayed by two PPARγ agonists, namely, troglitazone and rosiglitazone (Table W3). However, the fact that i) JLK1486 displays higher *in vitro* growth inhibitory activity than troglitazone and rosiglitazone (Figure 1*B*) and ii) JLK1486-induced effects on PPARγ activation are ranked seventh only among the 11 transcription factors whose activity is modified by JLK1486 (Table 1) strongly suggests that PPAR modulation is not the main mechanism by which JLK1486 exerts its cytostatic effects in glioma cells. In addition, the transient JLK1486-induced activation of PPARγ (Figure 4*C*) was not strong enough to decrease any cell cycle–related kinase activity, including CDK1, CDK2, and CDK4 (Table W2), whose activities are usually decreased on full PPARγ activation [35].

JLK1486 Activates Myt1 and STAT1

Data in Table 1 indicate that Myt1 and STAT1 may be important targets of JLK1486 in glioma cells in its cytostatic effects. We did not find three-dimensional structures of Myt1 in any databases, and we therefore focused our attention on STAT1, which was ranked second among 11 transcription factors targeted by JLK1486 (Table 1).

Molecular docking experiments revealed that both JLK1486 and Cpd30-12 (see Figure 1*A*), a selective ligand for STAT1 [34], displayed higher binding energy for STAT1 (JLK1486 = −11.4 kcal/mol; Cpd30-12 = −11.9 kcal/mol) than for STAT3 (JLK1486 = −9.6 kcal/mol; Cpd30-12 = −10.5 kcal/mol). On the basis of these data, it seems that JLK1486 displays a higher selectivity for STAT1 than Cpd30-12.

We first examined the best poses of Cpd30-12 docked in STAT1 (Figure 5*B*). The best solutions found are convergent if one considers the benzoic acid group of the ligand, whereas the heterocyclic ring has several possible poses. An H-bond appears between the ligand carboxylate and R602, whereas electrostatic interactions between E605, S606, A630, and E632 further stabilize the benzoic and the furyl rings (Figure 5*B*). One of the oxygens of the heterocycle presents an H-bond toward S606, whereas the receptor surface adapted its shape to fit the different poses with S604 and S606 side chain flexibility (Figure 5*B*). We then examined the best poses of JLK1486 docked in STAT1. The ligand lies in a groove, with the trifluoromethylbenzene

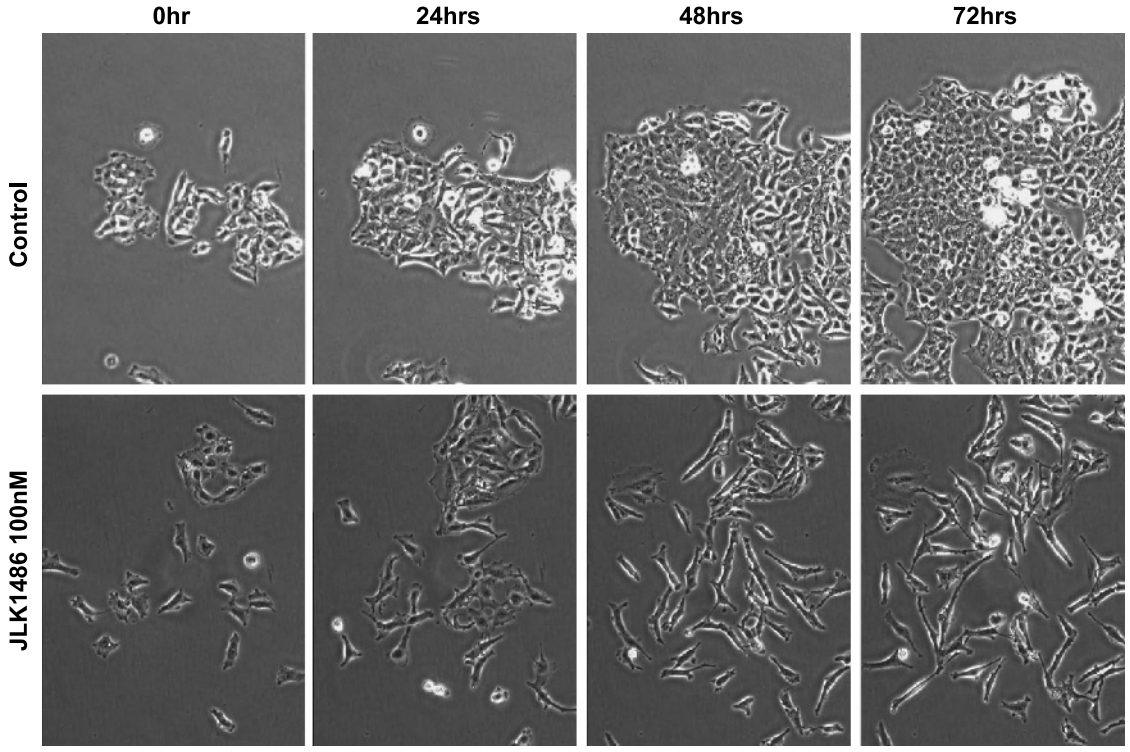

Figure 2. Morphologic illustrations of JLK1486-induced effects in human HS683 glioblastoma cells. Computer-assisted phase-contrast microscopy (quantitative videomicroscopy) was used to characterize the growth-inhibitory effects of JLK1486 in Hs683 glioblastoma cell populations. The top panel represents illustrations of Hs683 glioblastoma cells that were left untreated (control), whereas the bottom panel represents illustrations of Hs683 glioblastoma cells treated with 100 nM JLK1486.

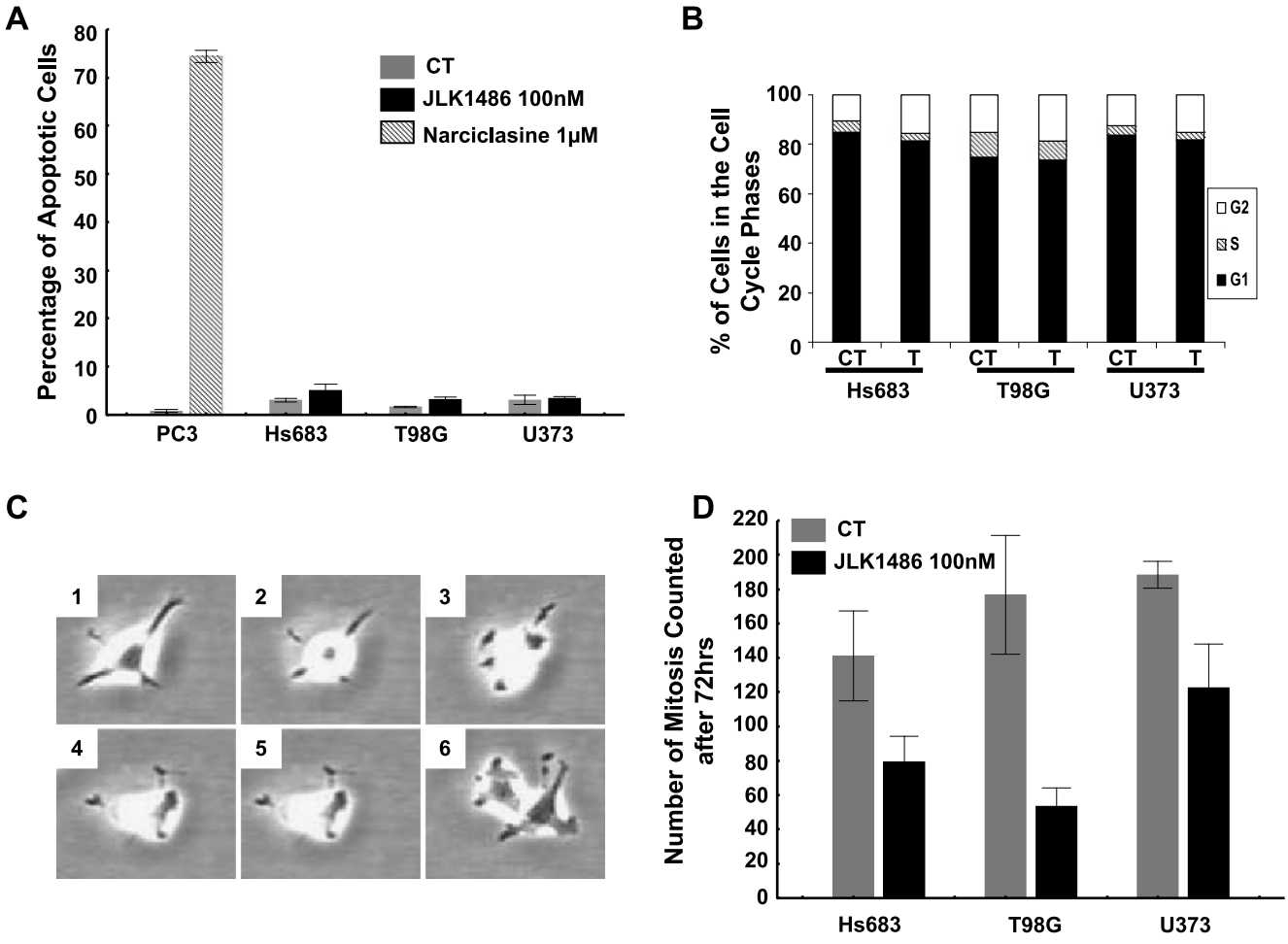

Figure 3. Analyses of JLK1486-induced effects in Hs683, U373, and T98G glioma cell proliferation *versus* apoptosis. (A) Flow cytometry analyses of apoptotic rates in glioma cells left untreated (control) or treated for 72 hours with 100 nM JLK1486; 1 μM narciclasine was used as a positive control (72 hours of treatment) in human PC3 prostate cancer cells. (B) Flow cytometry analyses of cell cycle kinetics (the percentages of cells in the G_1, S, and G_2 phases) in glioma cells left untreated (control) or treated for 72 hours with 100 nM JLK1486. (C) Illustrations of the morphological appearance of mitoses (M) in a U373 glioma cell population. (D) Quantitative videomicroscopy analyses of 100 nM JLK1486-induced effects on mitosis rates of glioma cells. Data are presented as mean ± SEM. Values were calculated in triplicate.

Table 1. JLK1486-Induced Effects at 100 nM for 24 Hours on the Activity of Various Transcription Factors.

Factor Name	Description	Function	T/CT
MyT1	Myelin transcription factor 1	Phosphorylates Cdc2	4.8
STAT1 p84/p91	Signal transducer and activator of transcription 1, 84 kDa (β)/91 kDa (α)	Antiproliferative/proapoptotic isoform STAT1α and proliferative isoform STAT1β play a crucial role in the regulation of cell cycle	4.1
ICSBP	Interferon consensus sequence binding protein (IRF-8)	Stable transfection with ICSBP inhibits lens carcinoma cell growth by upregulating caspase-1, $p21^{waf/cip1}$, and $p27^{Kip1}$ expression	3.5
v-Maf	v-*maf* musculoaponeurotic fibrosarcoma oncogene homolog (avian)	Overexpression of v-Maf activates p53 expression, which can lead to cell cycle arrest	3.1
C/EBP a/g	CCAAT/enhancer binding protein α, γ	Inhibits cell proliferation through $p21^{waf/cip1}$	2.8
WT1	Wilms tumor 1	Upregulates $p21^{waf/cip1}$ (inhibitor of G1/S progression) and downregulates cyclin E (promoter of cell cycle progression)	2.8
PPAR	Peroxisome proliferative–activated receptor	Inhibits proliferation through cyclin D1; cyclin-dependent kinases 1, 2, and 4, Ki-67, and proliferating cell nuclear antigen	2.8
IRF-1	Interferon regulatory factor 1	Expression of IRF-1 in different mammalian cell lines leads to down-regulation or stop of proliferation	2.3
NPAS2	Neuronal PAS domain protein 2	Knockdown of *NPAS2* in cancer cells represses the expression of FANCG (cell cycle checkpoint control) and MAPK2 (cell cycle arrest)	2.2
AP-2	Activating enhancer binding protein 2	Inhibits cancer cell growth and activates $p21^{waf/cip1}$ expression	2.1
HEN1	NHLH1 (nescient helix loop helix 1)	Prevents some postmitotic cells from reentering the cell cycle (neurogenesis)	2.0

T/CT indicates "treated/control."

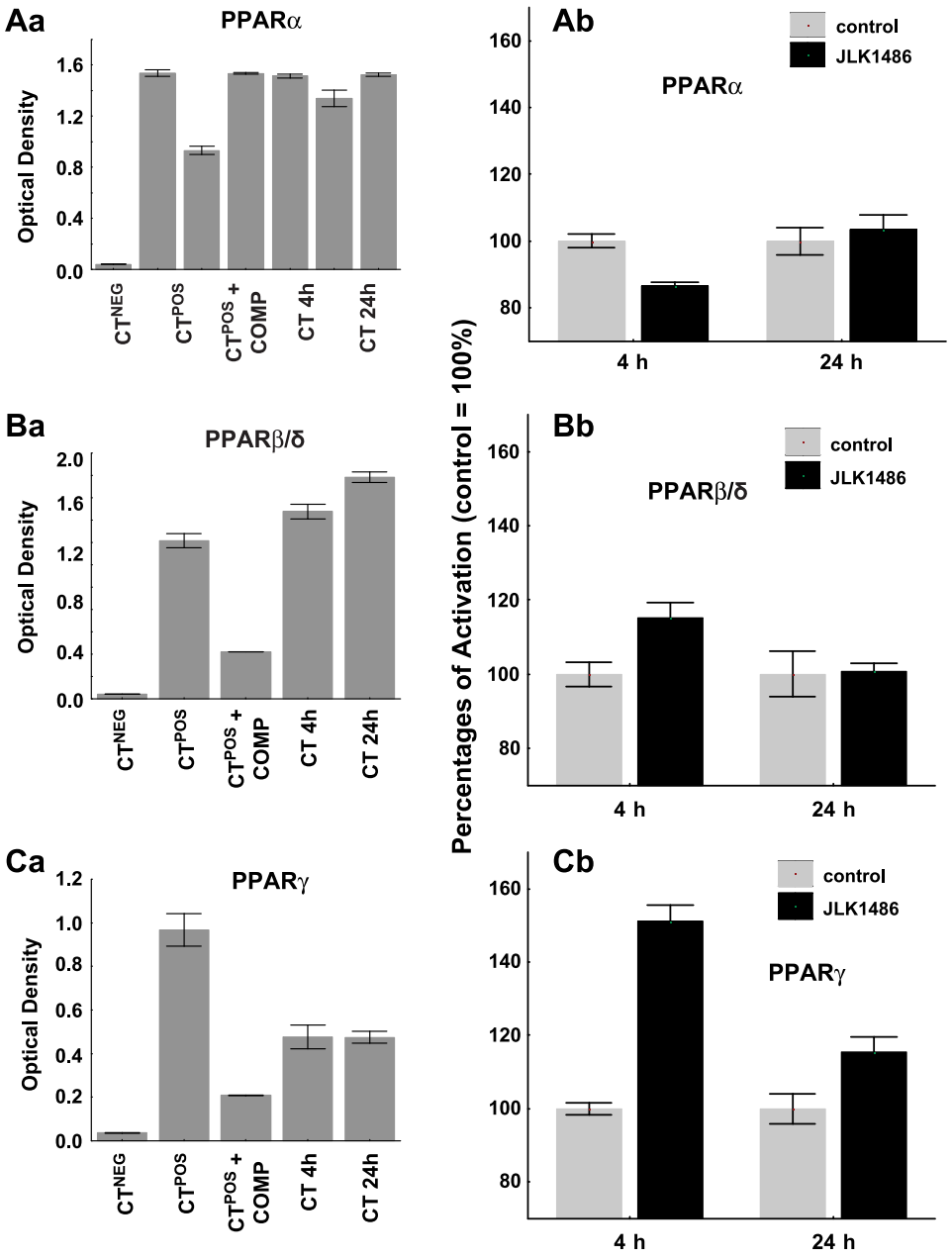

Figure 4. Characterization of the potential effects of JLK1486 on PPARα, β/δ, and γ activation. Whether JLK1486 (100 nM) is able to activate PPARs was investigated after 4 and 24 hours of treatment in U373 glioblastoma cells (Ab; Bb; Cb). The left panel represents the controls used to validate the assay (Aa; Ba; Ca). CT^{NEG} and CT^{POS} represent the negative and the positive controls, respectively, provided by the manufacturer. CT^{POS} + COMP represents an experimental condition in which a competitor (COMP) provided by the manufacturer was added in the same time than the CT^{POS}. CT 4h and CT 24h represent the control values in U373 glioma cells left untreated. There are these control values that have been arbitrarily normalized at 100% in the right panel. Data are presented as mean ± SEM. Values were calculated in triplicate.

pointing toward a polar pocket composed of K584, E587, R588, T615, and F628, forbidding further interaction with the pY binding site (Figure 5*C*). One of the quinoline rings is also directed toward K584 and makes an H-bond with S604 and T613 (Figure 5*C*). The other quinoline rings interact with D627, F628, and H629 as potentials hydrogen bonding residues, whereas the methyl side chain of A630 has an electrostatic effect with the aromatic ring (Figure 5*C*). Altogether, these data show that interactions of STAT1 with JLK1486 and Cpd30-12 are slightly different, but both ligands secure the pY binding site, whereas the hydrophobic pocket adapts its shape to the different molecules. We next performed the same analyses for STAT3; the data revealed that the ligand binding modes are quite different, suggesting that JLK1486 can probably inhibit any interaction with the pY binding site, whereas Cpd30-12 may not (data not shown).

Data presented in Figure 6 represent biochemical validations of the data presented in Table 1 and Figure 5. These data show that 100 nM JLK1486 markedly activated phospho-STAT1 in human U373 GBM cells after 24 hours of treatment and even slightly increased STAT1 protein expression (Figure 6*A*). We failed to demonstrate JLK1486-mediated activation of p21 because p21 is not expressed in human

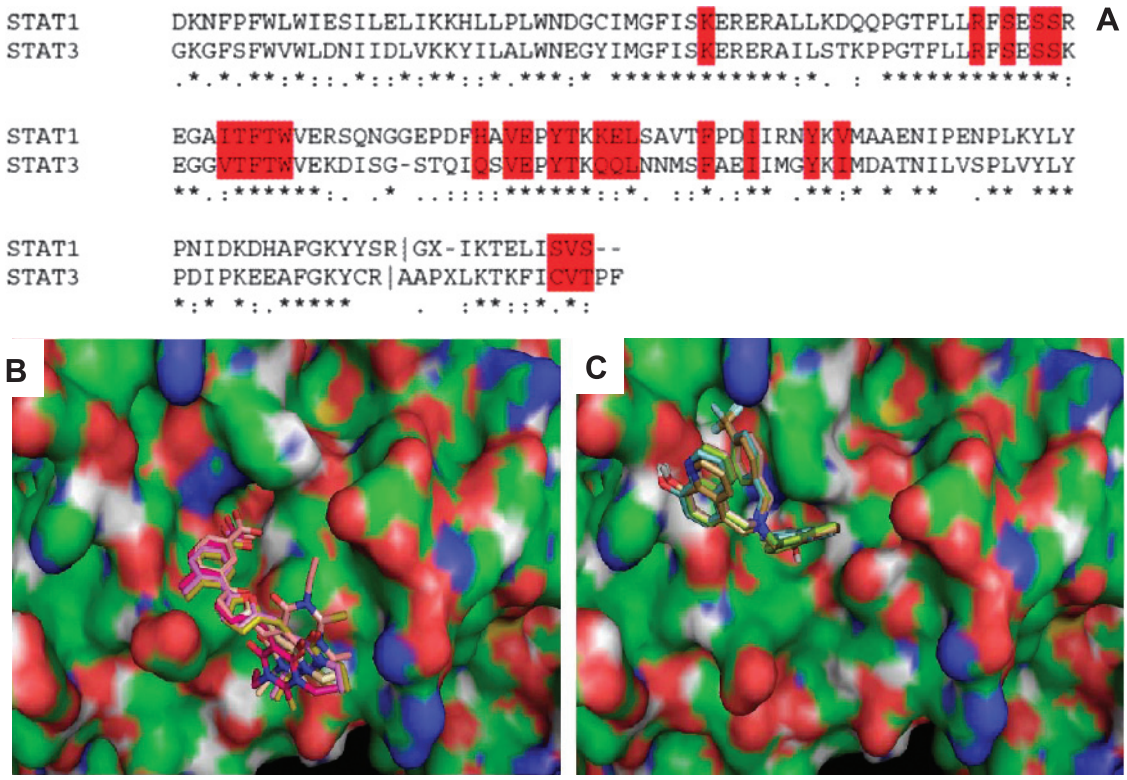

Figure 5. Docking of JLK1486 and Cpd30-12 in STAT1. (A) Sequence alignment of STAT1 and STAT3 (flexible residues are highlighted in red). (B) Consensus pose for Cpd30-12 is shown; electrostatic interactions with the receptor stabilize the benzoic ring and the heterocycle. The latter is able to adopt different orientations, whereas the aromatic ring is always in the same place (C). Consensus poses for JLK1486 stabilized by several H-bond and hydrophobic interactions. Illustrations were prepared with Pymol Molecular Graphics System (Version 1.2rl; Schrödinger, LLC).

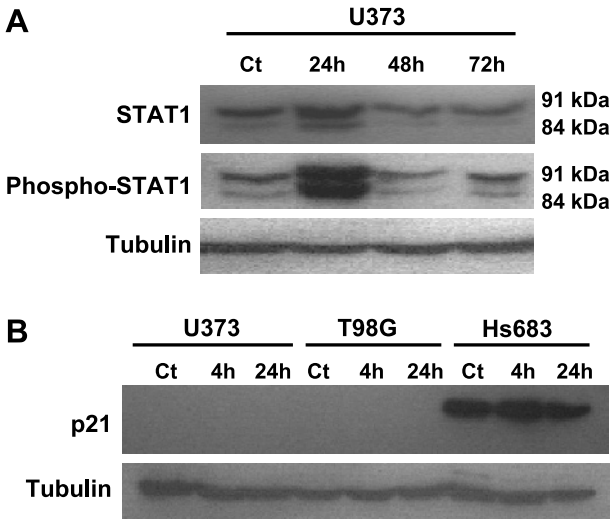

Figure 6. Characterization of the effects of JLK1486 on STAT1 and p21 activation. Western blot analyses of 100 nM JLK1486-mediated effects on levels of STAT1 expression and activation in human U373 GBM cells (A) and on levels of p21 expression in human U373, T98G, and Hs683 GBM cells (B). Tubulin was used as an internal control of protein quality. STAT1 exists in two forms: STAT1α (91 kDa) and STAT1β (84 kDa).

U373 and T98G GBM cell lines, whereas it is already expressed at very high levels in Hs683 GBM cells (Figure 6*B*).

JLK1486-Induced Antitumor Effects In Vivo

Figure 7 shows that long-term i.v. administration of 10 mg/kg JLK1486 contributed similar therapeutic benefits when compared with long-term i.v. administration of TMZ in a human Hs683 glioma model in which glioma cells are orthotopically xenografted into the brains of immunocompromised mice. The same features were observed when comparing chronic *per os* administrations of 20 mg/kg JLK1486 to 80 mg/kg TMZ (Figure 7).

Discussion

Despite a large number of new and sometimes very innovative approaches [20], treatment options for malignant gliomas, including glioblastomas, are still very limited [3,9], calling for further development of therapeutic strategies.

The current study relies on two previous studies from our group aimed at the development of novel hydroxyquinoline compounds as anticancer agents [21,36]. Hydroxyquinoline is a privileged structural moiety observed in many biologically active natural products, and it is used as a source for many drugs targeting a wide range of pathologies, including neurodegenerative, parasitic amoebic dysentery, and herpesvirus diseases [21]. We thus first reported preliminary

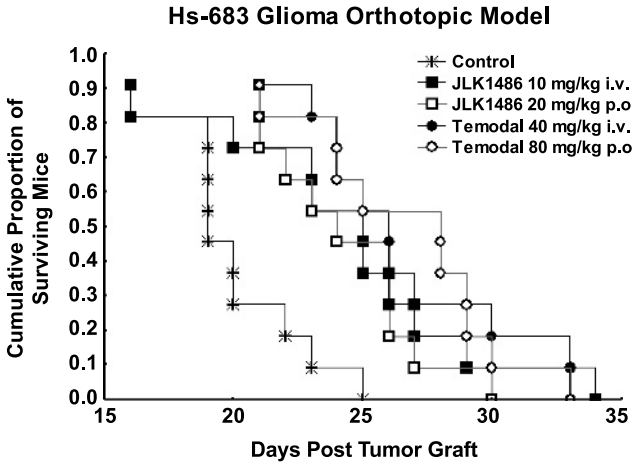

Figure 7. Characterization of the *in vivo* anticancer activity of JLK1486 *versus* TMZ (reference compound) in Hs683 xenografts. Human Hs683 glioblastoma cells were orthotopically grafted into the brains of immunocompromised mice (11 mice per experimental group). The mice in the control group were left untreated, whereas the mice of the four remaining groups were treated either orally (p.o.) or intravenously (i.v.) with JLK1486 and TMZ three times a week (Monday, Wednesday, Friday) for three consecutive weeks, with treatment starting on the fifth day after graft.

data on the anticancer activity of a family of bis 8-hydroxyquinoline–substituted benzylamines [36]. We then enlarged the initial panel of these bis 8-hydroxyquinoline benzylamine analogs to proceed with SAR analyses for *in vitro* anticancer activity; JLK1486 seemed as a potential hit in anticancer activity, at least *in vitro* [21]. Our previous study also pointed to the fact that JLK1486-induced anticancer activity occurred through cytotoxic effects in carcinoma cells, whereas this anticancer activity of JLK1486 turned out to be cytostatic in U87 glioma cells *in vitro* [21]. The present study confirms the cytostatic effects of JLK1486 in Hs683, T98G, and U373 glioma cells. The present study further reveals that these JLK1486-mediated cytostatic effects seem to occur, at least partly, through the activation of various transcription factors that in turn activate antiproliferative genes (Table 1). In contrast, JLK1486 does not seem to directly target kinases (Table W2).

PPARγ could be one of the transcription factors activated by JLK1486. Molecular docking experiments revealed similar potential affinity for PPARγ when compared with two thiazolidinediones (TDZs), namely, troglitazone and rosiglitazone (Table W3). As emphasized by Seufert et al. [37], there is increasing evidence that PPARγ agonists, including TDZs and non-TDZs, block the motility and invasiveness of glioma cells. GW7845, an investigational non-TDZ PPARγ ligand, binds and activates human PPARγ at nanomolar concentrations and thus possesses a higher potency than TDZs, such as pioglitazone, troglitazone, rosiglitazone, and the experimental PPARγ agonist ciglitazone, which require submicromolar doses [37]. Grommes et al. [38] demonstrated that 30 μM GW7845 reduced the viability of rat C6 and human U87 and A172 glioma cells through cell cycle arrest and increased cell death. The data presented here show that these effects are achieved with 0.1 μM JLK1486 [38]. Grommes et al. [38] also demonstrated for the first time that the activation of PPARγ by GW845 leads to inhibition of the migration and invasion abilities of C6 rat glioma cells *in vitro*. A subsequent study revealed that the FDA-approved TDZ pioglitazone exhibits antiglioma properties similar to GW7845 [37]. Ciglitazone also induces apoptosis in glioma cells [39]. Apart from the cytostatic effects we report here for JLK1486, we also observed that this compound markedly impaired Hs683, T98G, and U373 glioma cell migration at concentrations below 0.1 μM *in vitro* (data not shown), as revealed by quantitative videomicroscopy-related wound healing assays [29]. However, if PPARγ could be one of the antiproliferative transcription factors activated by JLK1486, it seems obvious that PPARγ is not the sole target of JLK1486 (Table 1).

The major antiproliferative transcription factor targeted by JLK1486 seems to be Myt1 (Table 1), which controls the progress of cells into and out of mitosis [40]. Myt1 also helps cancer cells to react against the adverse effects of chemotherapeutic agents through G_2 arrest [41]. We did not investigate Myt1 in the present study because we were unable to visualize Myt1-JLK1486 interactions because of a lack of available three-dimensional Myt1 structures in protein databases. We are currently developing an original pharmacological approach aimed at characterizing how JLK1486 modulates Myt1 activity in glioma cells.

Another major candidate for JLK1486's cytostatic effects is STAT1 (Table 1 and Figure 6*A*). Signal transducers and activators of transcription (STATs) are latent cytoplasmic transcription factors that mediate various biologic responses, such as cell proliferation, survival, apoptosis, and differentiation [42]. Seven STATs are known in mammals, that is, STAT1, STAT2, STAT3, STAT4, STAT5A, STAT5B, and STAT6 [43].

STAT1 is usually considered to be a tumor suppressor, whereas STAT3 is considered an oncogene, and its constitutive inactivation is reported in nearly 70% of solid and hematological tumors [44]. Indeed, dysregulation of STAT1 signaling seems to be associated with the development of cancer [42]. However, if it is true that STAT1-deficient mice spontaneously develop tumors, the fact also remains that constitutively activated STAT1 signaling is present in a number of human cancers [45]. In contrast to STAT1, inhibition of persistent STAT3 activation by blocking tyrosine kinase activity has been repeatedly associated with selective tumor growth suppression and cell death [45].

On cytokine and growth factor stimulation, cytoplasmic STAT molecules become activated through tyrosine phosphorylation, dimerize through reciprocal phosphotyrosine (pTyr)–SH2 interactions, accumulate in the nucleus, bind to DNA, and activate gene transcription [43]. Subsequent inactivation involves phospho-STATs dissociating from DNA, becoming dephosphorylated, and exported to the cytoplasm [43]. STAT1 and STAT3 activation is reciprocally regulated, and perturbation of their expression or phosphorylation levels may redirect cytokine/growth factor signals from proproliferative to proapoptotic [44]. In fact, both STAT1 and STAT3 can exert their opposing effects on tumorigenesis either directly, through transcriptional regulation of target genes in the cancer cells, or indirectly, by modulating tumor angiogenesis or the antitumor immune response [44].

Accumulating evidence now supports an important role for STAT1 in various forms of cell death, encompassing both apoptotic and nonapoptotic pathways [42]. STAT1-dependent apoptosis is mediated by the induction of the interferon regulatory factor 1 (IRF-1) and involves regulation of the expression of members of the cell surface death receptor family and their ligands, namely, Fas, FasL, TNF-related apoptosis–inducing ligand and its receptor KILLER/DR5, caspases, both at the basal level and on stimulation by cytokines and iNOS [44]. STAT1 also negatively regulates the cell cycle by inducing the CDK inhibitors $p21^{waf/cip1}$ and $p27^{Kip-1}$ and by downregulating the expression of c-*myc* and several cyclins [44]. Data in Figure 6*A* confirm these data by illustrating the fact that JLK1486 actually activates STAT1.

Data in Table 1 show that, apart from activating STAT1, JLK1486 also activated four other growth factors that directly or indirectly activate $p21^{waf/cip1}$, namely, AP-2, WT1, C/EBPa/g, and ICSBP. Thus, data presented here show that JLK1486 activates STAT1 (Table 1 and Figure 6*A*) and molecular docking experiments strongly suggest a higher selectivity of JLK1486 for STAT1 than for STAT3 (Figure 5). Moreover, the data argue in favor of the fact that JLK1486-induced activation of STAT1 leads to negative regulation of the cell cycle (and thus to cytostatic effects) rather than to the activation of apoptosis (and thus to cytotoxic effects). Indeed, JLK1486 impairs glioma cell proliferation, whereas not resulting in cell death, during a frame of 3 days of observation (Figures 2 and 3). Glioma cell death occurs 7 days after JLK1486 treatment at its IC_{50} growth-inhibitory concentration (data not shown), a feature that is likely a consequence of prolonged cell growth arrest rather than direct cell killing.

So far, drugs that activate STAT1 rather than inhibit STAT1 signaling have not been characterized. Finding such drugs would be very interesting and JLK1486 could be such a candidate. However, it is difficult to mechanistically understand how a drug binding to the SH-2 domain of STAT1 could activate STAT1 rather than act as an inhibitor. In fact, the drug Cpd30-12, which, by modeling, was linked to similar docking site as JLK1486, is a described inhibitor of STAT1 rather than an activator [34]. It must be emphasized that in our hand, Cpd30-12 binding pose differed slightly from the one already reported [34]: the benzoic acid group points toward R602 with our model, a feature that can be accounted to the allowed flexibility of the receptor in our study, leading to different poses.

We will pay a particular attention to STAT1 in the next experiments we will perform with JLK1486 to further decipher its mechanisms of anticancer action. In the same manner, we did not yet experimentally explore the effect of JLK1486 to the related STAT3, which might be also a potential relevant target, and these experiments will also be conducted in the next steps because the role of STAT3 in gliomas is already well documented [46].

In conclusion, whether the observed activation of various transcription factors (Myt1, STAT1, and PPARγ) by JLK1486 is due to a general up-regulation of stress pathways in the glioma cells after drug treatment or directly linked to the cytostatic action of the drug remains an open question. However, the data of the current study clearly point to the fact that JLK1486 exerts cytostatic, not cytotoxic, effects in glioma cells. JLK1486 mediated anticancer activity *in vivo* (through i.v. as well as oral routes of administrations) in an orthotopic human glioma xenograft model with efficiency similar to that of TMZ, the criterion standard in glioma treatment. Whether such compounds could provide additive *versus* synergistic effects in combination with TMZ remains to be determined.

Acknowledgments

The authors thank Jean-François Gaussin, Fabrice Ribaucour, Mischael Dehoux, and Aline Marcowycz for excellent technical assistance.

References

[1] Sanai N, Alvarez-Buylla A, and Berger MS (2005). Neural stem cells and the origin of gliomas. *N Engl J Med* **353**, 811–822.

[2] Louis DN (2006). Molecular pathology of malignant gliomas. *Annu Rev Pathol Mech Dis* **1**, 97–117.

[3] Lefranc F, Facchini V, and Kiss R (2007). Proautophagic drugs: a novel means to combat apoptosis-resistant cancers, with a special emphasis on glioblastomas. *Oncologist* **12**, 1395–1403.

[4] Rao JS (2003). Molecular mechanisms of glioma invasiveness: the role of proteases. *Nat Rev Cancer* **3**, 489–501.

[5] Lefranc F, Brotchi J, and Kiss R (2005). Possible future issues in the treatment of glioblastomas, with a special emphasis on cell migration and the resistance of migrating glioblastoma cells to apoptosis. *J Clin Oncol* **23**, 2411–2422.

[6] Sontheimer H (2008). An unexpected role for ion channels in brain tumor metastasis. *Exp Biol Med (Maywood)* **233**, 779–791.

[7] Lefranc F and Kiss R (2008). The sodium pump α-1 subunit as a potential target to combat apoptosis-resistant glioblastomas. *Neoplasia* **10**, 198–206.

[8] Ceruti S, Mazzola A, and Abbrachio MP (2005). Resistance of human astrocytomas cells to apoptosis induced by mitochondria-damaging agents: possible implications for anticancer therapy. *J Pharmacol Exp Ther* **314**, 825–837.

[9] Stupp R, Hegi ME, Mason WP, van den Bent MJ, Taphoorn MJ, Janzer RC, Ludwin SK, Allgeier A, Fisher B, Belanger K, et al. (2009). Effects of radiotherapy with concomitant and adjuvant temozolomide *versus* radiotherapy alone on survival in glioblastoma in a randomized phase III study: 5-year analysis of the EORTC-NCIC trial. *Lancet Oncol* **10**, 459–466.

[10] Chakravarti A, Erkkinen MG, Nestler U, Stupp R, Mehta M, Aldape K, Gilbert MR, Black PM, and Loeffler JS (2006). Temozolomide-mediated radiation enhancement in glioblastoma: a report on underlying mechanisms. *Clin Cancer Res* **12**, 4738–4746.

[11] Kanzawa T, Germano IM, Komata T, Ito H, Kondo Y, and Kondo S (2004). Role of autophagy in temozolomide-induced cytotoxicity for malignant glioma cells. *Cell Death Differ* **11**, 448–457.

[12] Katayama M, Kawaguchi T, Berger MS, and Pieper RO (2007). DNA damaging agent–induced autophagy produces a cytoprotective adenosine triphosphate surge in malignant glioma cells. *Cell Death Differ* **14**, 548–558.

[13] Roos WP, Batista LFZ, Naumann SC, Wick W, Weller M, Menck CFM, and Kaina B (2007). Apoptosis in malignant glioma cells triggered by the temozolomide-induced DNA lesion O^6-methylguanine. *Oncogene* **26**, 186–197.

[14] Mathieu V, De Nève N, Le Mercier M, Dewelle J, Gaussin JF, Dehoux M, Kiss R, and Lefranc F (2008). Combining bevacizumab with temozolomide increases the antitumor efficacy of temozolomide in a human glioblastoma orthotopic xenograft model. *Neoplasia* **10**, 1383–1392.

[15] Hegi ME, Liu L, Herman JG, Stupp R, Wick W, Weller M, Mehta MP, and Gilbert MR (2008). Correlation of O^6-methylguanine methyltransferase (MGMT) promoter methylation with clinical outcomes in glioblastoma and clinical strategies to modulate MGMT activity. *J Clin Oncol* **26**, 4189–4199.

[16] Le Calvé B, Rynkowski M, Le Mercier M, Bruyère C, Lonez C, Gras T, Haibe-Kains B, Bontempi G, Decaestecker C, Ruyschaert JM, et al. (2010). Long-term *in vitro* treatment of human glioblastoma cells with temozolomide increases resistance *in vivo* through up-regulation of GLUT transporter and aldo-keto reductase enzyme AKR1C expression. *Neoplasia* **12**, 727–739.

[17] Lamoral-Theys D, Le Mercier M, Le Calvé B, Rynkowski M, Bruyère C, Decaestecker C, Haibe-Kains B, Bontempi G, Dubois J, Lefranc F, et al. (2010). Long-term temozolomide treatment induces marked amino metabolism modifications and an increase in TMZ sensitivity in Hs683 oligodendroglioma cells. *Neoplasia* **12**, 69–79.

[18] Franceschi E, Omuro AM, Lassman AB, Demopoulos A, Nolan C, and Abrey LE (2005). Salvage temozolomide for prior temozolomide responders. *Cancer* **104**, 2473–2476.

[19] Furnari FB, Fenton T, Bachoo RM, Mukasa A, Stommel JM, Stegh A, Hahn WC, Ligon KL, Louis DN, Brennan C, et al. (2007). Malignant astrocytic glioma: genetics, biology, and paths to treatment. *Genes Dev* **21**, 2683–2710.

[20] Djedid R, Kiss R, and Lefranc F (2009). Targeted therapy of glioblastomas: a 5-year view. *Future Med* **6**, 351–370.

[21] Madonna S, Béclin C, Laras Y, Moret V, Marcowycz A, Lamoral-Theys D, Dubois J, Barthelemy-Requin M, Lenglet G, Depauw S, et al. (2010). Structure-activity relationships and mechanism of action of antitumor bis 8-hydroxyquinoline substituted benzylamines. *Eur J Med Chem* **45**, 623–638.

[22] Wang P, Song Y, Zhang L, He H, and Zhou X (2005). Quinone methide derivatives: important intermediates to DNA alkylating and DNA cross-linking actions. *Curr Med Chem* **12**, 2893–2913.

[23] Branle F, Lefranc F, Camby I, Jeuken J, Geurts-Moespot A, Sprenger S, Sweep F, Kiss R, and Salmon I (2002). Evaluation of the efficiency of chemotherapy in *in vivo* orthotopic models of human glioma cells with and without 1p/19q deletions and in C6 rat orthotopic allografts serving for the evaluation of surgery combined with chemotherapy. *Cancer* **95**, 641–655.

[24] Le Mercier M, Fortin S, Mathieu V, Roland I, Spiegl-Kreinecker S, Haibe-Kains B, Bontempi G, Decaestecker C, Berger W, Lefranc F, et al. (2009). Galectin-1

proangiogenic and promigratory effects in the Hs683 oligodendroglioma model are partly mediated through the control of BEX2 expression. *Neoplasia* **11**, 485–496.

[25] Lefranc F, James S, Camby I, Gaussin JF, Darro F, Brotchi J, Gabius HJ, and Kiss R (2005). Combined cimetidine and temozolomide, compared with temozolomide alone: significant increases in survival in nude mice bearing U373 human glioblastoma multiforme orthotopic xenograft. *J Neurosurg* **102**, 706–714.

[26] Ingrassia L, Lefranc F, Dewelle J, Pottier L, Mathieu V, Spiegl-Kreinecker S, Sauvage S, El Yazidi M, Dehoux M, Berger W, et al. (2009). Structure-activity-relationship analysis of novel derivatives of narciclasine (an Amaryllidaceae isocarbostyril alkaloid) as potential anti-cancer agents. *J Med Chem* **52**, 1100–1114.

[27] Lefranc F, Mijatovic T, Kondo Y, Sauvage S, Roland I, Krstic D, Vasic V, Gailly P, Kondo S, Blanco G, et al. (2008). Targeting the α-1 subunit of the sodium pump (the Na^+/K^+-ATPase) to combat glioblastoma cells. *Neurosurgery* **62**, 211–222.

[28] Mathieu V, Le Mercier M, De Neve N, Sauvage S, Gras T, Roland I, Lefranc F, and Kiss R (2007). Galectin-1 knockdown increases sensitivity to temozolomide in a B16F10 mouse metastatic melanoma model. *J Invest Dermatol* **127**, 2399–2410.

[29] Debeir O, Mégalizzi V, Warzée N, Kiss R, and Decaestecker C (2008). Videomicroscopic extraction of specific information on cell proliferation and migration *in vitro*. *Exp Cell Res* **314**, 2985–2998.

[30] Lamoral-Theys D, Pottier L, Kerff F, Dufrasne F, Proutière F, Wauthoz N, Neven P, Ingrassia L, Van Antwerpen P, Lefranc F, et al. (2010). Simple di- and trivanillates exhibit cytostatic properties toward cancer cells resistant to pro-apoptotic stimuli. *BioOrg Med Chem* **18**, 3823–3833.

[31] Mathieu V, Mijatovic T, Van Damme M, and Kiss R (2005). Gastrin exerts pleitropic effects on human melanoma cell biology. *Neoplasia* **7**, 930–943.

[32] Trott O and Olson AJ (2010). AutoDock Vina: improving the speed and accuracy of docking with a new scoring function, efficient optimization, and multithreading. *J Comput Chem* **31**, 455–461.

[33] Sanner MF (1999). Python: a programming language for software integration and development. *J Mol Graphics Mod* **17**, 57–61.

[34] Xu X, Kasembeli MM, Jiang X, Tweardy BJ, and Tweardy DJ (2009). Chemical probes that competitively and selectively inhibit Stat3 activation. *PLoS One* **4**(3), e4783.

[35] Ondrey F (2009). Peroxisome proliferator–activated receptor gamma pathway targeting in carcinogenesis: implications for chemoprevention. *Clin Cancer Res* **15**, 2–8.

[36] Moret V, Laras Y, Cresteil T, Aubert G, Di QPDC, Barthelemy-Requin M, Beclin C, Peyrot V, Allegro D, Rolland A, et al. (2009). Discovery of a new family of bis-8-hydroxyquinoline substituted benzylamines with pro-apoptotic activity in cancer cells: synthesis, structure-activity relationship, and action mechanism studies. *Eur J Med Chem* **44**, 558–567.

[37] Seufert S, Coras R, Tränkle C, Zlotos DP, Blümcke I, Tatenhorst L, Heneka MT, and Hahnen E (2008). PPARγ activators: off-target against glioma cell migration and brain invasion. *PPAR Res* **2008**, 513943.

[38] Grommes C, Landreth GE, Schlegel U, and Heneka MT (2005). The nonthiazolinidinedione tyrosine–based peroxisome proliferator–activated receptor gamma ligand GW7845 induces apoptosis and limits migration and invasion of rat and human glioma cells. *J Pharmacol Exp Ther* **313**, 806–813.

[39] Strakova N, Ehrmann J, Dzubak P, Bouchal J, and Kolar Z (2004). The synthetic ligand of peroxisome proliferator–activated receptor-γ ciglitazone affects human glioblastoma cell lines. *J Pharmacol Exp Ther* **309**, 1239–1247.

[40] Potapova TA, Daum JR, Byrd KS, and Gorbsky GJ (2009). Fine tuning the cell cycle: activation of the Cdk1 inhibitory phosphorylation pathway during mitotic exit. *Mol Biol Cell* **20**, 1737–1748.

[41] Wang Y, Decker SJ, and Sebolt-Leopold J (2004). Knockdown of Chk1, Wee1 and Myt1 by RNA interference abrogates G_2 checkpoint and induces apoptosis. *Cancer Biol Ther* **3**, 305–313.

[42] Kim HS and Lee MS (2007). STAT1 as a key modulator of cell death. *Cell Signal* **19**, 454–465.

[43] Mao X, Ren Z, Parker GN, Sondermann H, Pastorello MA, Wang W, McMurray JS, Demeler B, Darnell JE Jr, and Chen X (2005). Structural bases of unphosphorylated STAT1 association and receptor binding. *Mol Cell* **17**, 761–771.

[44] Regis G, Pensa S, Boselli D, Novelli F, and Poli V (2008). Ups and downs: the STAT1:STAT3 seesaw of interferon and gp130 receptor signaling. *Sem Cell Dev Biol* **19**, 351–359.

[45] Gunning PT, Katt WP, Glenn M, Siddique K, Kim JS, Jove R, Sebti SM, Turkson J, and Hamilton AD (2007). Isoform selective inhibition of STAT1 or STAT3 homo-dimerization via peptidomimetic probes: structural recognition of STAT SH2 domains. *Bioorg Med Chem Lett* **17**, 1875–1878.

[46] Atkinson GP, Nozell SE, and Benveniste ET (2010). NF-κB and STAT3 signaling in glioma: targets for future therapies. *Expert Rev Neurother* **10**, 575–586.

Table W1. List of Kinase and Substrates and Experimental Protocol and References.

No.	Kinase	Lot	Conc. (ng/50 µl)	Substrate	Lot	Conc. (µg/50 µl)
1	ABL1 T315I	2	50	Poly(Ala,Glu,Lys,Tyr)6:2:5:1	SIG_53H5516	0.25
2	ABL1 wt	3	25	Poly(Ala,Glu,Lys,Tyr)6:2:5:1	SIG_53H5516	0.125
3	ABL2	1	20	Poly(Glu,Tyr)4:1	SIG_20K5903	0.25
4	ACK1	3	50	Poly(Glu,Tyr)4:1	SIG_20K5903	0.125
5	ACV-R1	1	20	GSK3(14-27)	8	2
6	ACV-R1B	2	5	RBER-CHKtide	24	4
7	ACV-RL1	1	20	Casein	SIG_83K7430	1
8	AKT1	7	25	GSK3(14-27)	8	2
9	AKT2	3	200	GSK3(14-27)	6	1
10	ALK	2	25	Poly(Glu,Tyr)4:1	SIG_20K5903	0.125
11	AMPK-alpha1 fl	1	200	RBER-CHKtide	23	2
12	Aurora-A	4	50	tetra(LRRWSLG)	5	0.5
13	Aurora-B	7	100	tetra(LRRWSLG)	5	0.25
14	Aurora-C	8	200	tetra(LRRWSLG)	4	0.25
15	AXL	3	50	Poly(Glu,Tyr)4:1	SIG_20K5903	0.25
16	BLK	1	100	Poly(Glu,Tyr)4:1	SIG_20K5903	0.125
17	BMX	3	20	Poly(Glu,Tyr)4:1	SIG_20K5903	0.25
18	B-RAF V600E	1	25	MEK1-KM (kinase-dead)	21	0.5
19	B-RAF wt	1	20	MEK1-KM (kinase-dead)	22	0.5
20	BRK	4	25	Poly(Glu,Tyr)4:1	SIG_20K5903	0.125
21	BRSK1	1	3	RBER-CHKtide	24	2
22	BTK	2	25	Poly(Glu,Tyr)4:1	SIG_20K5903	0.125
23	CAMK1D	1	100	RBER-CHKtide	24	1
24	CAMK2A	1	2	RBER-CHKtide	23	2
25	CAMK2B	1	100	RBER-CHKtide	022.1	2
26	CAMK2D	1	2	RBER-CHKtide	022.1	2
27	CAMK4	1	150	JUN	3	0.5
28	CAMKK2	1	10	GSK3(14-27)	6	2
29	CDC42BPA	1	10	S6-peptide	4	1
30	CDC42BPB	1	25	S6-peptide	4	1
31	CDK1/CycA	5	10	RBER-CHKtide	22	2
32	CDK1/CycB1	25	25	RBER-CHKtide	24	2
33	CDK1/CycE	1	50	RBER-CHKtide	22	2
34	CDK2/CycA	5	25	RBER-CHKtide	24	1
35	CDK2/CycE	9	10	RBER-CHKtide	9	1
36	CDK3/CycE	1	10	RBER-CHKtide	23	1
37	CDK4/CycD1	7	20	RBER-CHKtide	24	2
38	CDK4/CycD3	1	10	RBER-CHKtide	24	1
39	CDK5/p25NCK	1	15	RBER-CHKtide	24	1
40	CDK5/p35NCK	1	15	RBER-CHKtide	24	1
41	CDK6/CycD1	4	200	RBER-CHKtide	24	2
42	CDK7/CycH/MAT1	2	25	RBER-CHKtide	24	2
43	CDK8/CycC	2	50	RBER-CHKtide	1	1
44	CDK9/CycT	4	15	RBER-CHKtide	22	1
45	CHK1	2	50	RBER-CHKtide	17	2
46	CHK2	2	10	tetra(LRRWSLG)	4	0.5
47	CK1-alpha1	1	100	Casein	SIG_65K7410	1
48	CK1-delta	1	5	Casein	SIG_65K7410	1
49	CK1-epsilon	1	2,5	Casein	SIG_83K7430	0.5
50	CK1-gamma1	1	5	Casein	SIG_65K7410	1
51	CK1-gamma2	1	5	Casein	SIG_83K7430	1
52	CK1-gamma3	1	5	Casein	SIG_83K7430	1
53	CK2-alpha1	3	20	Casein	SIG_83K7430	1
54	CK2-alpha2	1	50	Casein	SIG_65K7410	1
55	CLK1	1	400	H2O (Autophos.)	0	0
56	COT	18	300	RBER-CHKtide	24	3
57	CSF1-R	4	25	Poly(Glu,Tyr)4:1	SIG_20K5903	0.125
58	CSK	1	20	Poly(Glu,Tyr)4:1	SIG_20K5903	0.125
59	DAPK1	2	40	GSK3(14-27)	8	2
60	DAPK2	1	10	S6-peptide	4	2
61	DAPK3	1	5	GSK3(14-27)	6	2
62	DCAMKL2	1	10	RBER-CHKtide	24	1
63	DDR2	2	50	Poly(Ala,Glu,Lys,Tyr)6:2:5:1	SIG_53H5516	0.25
64	DMPK	1	200	tetra(LRRWSLG)	5	2
65	DYRK1A	2	5	RBER-CHKtide	24	2
66	DYRK1B	1	2	RBER-CHKtide	23	2
67	EEF2K	1	1	GSK3(14-27)	6	4
68	EGF-R L858R	1	5	Poly(Glu,Tyr)4:1	SIG_20K5903	0.25
69	EGF-R T790M	1	10	Poly(Glu,Tyr)4:1	SIG_20K5903	0.125
70	EGF-R T790M/L858R	1	10	Poly(Glu,Tyr)4:1	SIG_20K5903	0.125
71	EGF-R wt	15	10	Poly(Glu,Tyr)4:1	SIG_20K5903	0.125
72	EIF2AK2	2	10	Rb-CTF	13	1
73	EIF2AK3	1	10	MEK1-KM (kinase-dead)	SIG_83K7430	2

Table W1. (*continued*)

No.	Kinase	Lot	Conc. (ng/50 µl)	Substrate	Lot	Conc. (µg/50 µl)
74	EPHA1	1	50	Poly(Glu,Tyr)4:1	SIG_20K5903	0.125
75	EPHA2	1	20	Poly(Glu,Tyr)4:1	SIG_20K5903	0.125
76	EPHA3	1	150	Poly(Glu,Tyr)4:1	SIG_20K5903	0.25
77	EPHA4	1	150	Poly(Glu,Tyr)4:1	SIG_20K5903	0.25
78	EPHA5	1	5	Poly(Glu,Tyr)4:1	SIG_20K5903	0.5
79	EPHA7	1	20	Poly(Glu,Tyr)4:1	SIG_20K5903	0.125
80	EPHA8	1	20	Poly(Glu,Tyr)4:1	SIG_20K5903	0.125
81	EPHB1	1	20	Poly(Glu,Tyr)4:1	SIG_20K5903	0.125
82	EPHB2	6	100	Poly(Ala,Glu,Lys,Tyr)6:2:5:1	SIG_53H5516	0.125
83	EPHB3	1	25	Poly(Glu,Tyr)4:1	SIG_20K5903	0.125
84	EPHB4	7	10	Poly(Glu,Tyr)4:1	SIG_20K5903	0.125
85	ERBB2	12	100	Poly(Glu,Tyr)4:1	SIG_20K5903	0.125
86	ERBB4	7	40	Poly(Glu,Tyr)4:1	SIG_20K5903	0.125
87	ERK1	2	5	RBER-CHKtide	24	2
88	ERK2	4	10	RBER-CHKtide	24	2
89	FAK	15	40	Poly(Glu,Tyr)4:1	SIG_20K5903	0.125
90	FER	2	10	Poly(Glu,Tyr)4:1	SIG_20K5903	0.125
91	FES	2	5	Poly(Glu,Tyr)4:1	SIG_20K5903	0.125
92	FGF-R1 V561M	2	10	Poly(Ala,Glu,Lys,Tyr)6:2:5:1	SIG_53H5516	0.25
93	FGF-R1 wt	11	40	Poly(Glu,Tyr)4:1	SIG_20K5903	0.125
94	FGF-R2	1	5	Poly(Glu,Tyr)4:1	SIG_20K5903	0.125
95	FGF-R3	4	100	Poly(Glu,Tyr)4:1	SIG_20K5903	0.125
96	FGF-R4	6	50	Poly(Glu,Tyr)4:1	SIG_20K5903	0.125
97	FGR	1	50	Poly(Glu,Tyr)4:1	SIG_20K5903	50
98	FLT3 D835Y	3	10	Poly(Ala,Glu,Lys,Tyr)6:2:5:1	SIG_53H5516	0.5
99	FLT3 ITD	1	100	Poly(Ala,Glu,Lys,Tyr)6:2:5:1	SIG_53H5516	0.125
100	FLT3 wt	11	50	Poly(Ala,Glu,Lys,Tyr)6:2:5:1	SIG_53H5516	0.125
101	FRK	1	25	Poly(Glu,Tyr)4:1	SIG_20K5903	0.5
102	FYN	2	10	Poly(Glu,Tyr)4:1	SIG_20K5903	0.125
103	GRK2	1	50	Casein	SIG_65K7410	0.5
104	GRK3	1	10	Casein	SIG_65K7410	2
105	GRK4	1	5	Casein	SIG_65K7410	0.5
106	GRK5	1	5	Casein	SIG_83K7430	1
107	GRK6	2	10	Casein	SIG_65K7410	1
108	GSK3-alpha	1	50	RBER-CHKtide	24	4
109	GSK3-beta	3	50	RBER-CHKtide	24	1
110	HCK	1	25	Poly(Glu,Tyr)4:1	SIG_20K5903	0.125
111	HIPK1	1	20	RBER-CHKtide	24	2
112	HIPK3	1	20	RBER-CHKtide	24	2
113	HRI	1	100	Casein	SIG_83K7430	0.5
114	IGF1-R	12	20	Poly(Glu,Tyr)4:1	SIG_20K5903	0.125
115	IKK-alpha	3	50	RBER-CHKtide	23	2
116	IKK-beta	5	100	RBER-CHKtide	24	1
117	IKK-epsilon	6	20	GSK3(14-27)	8	1
118	INS-R	6	10	Poly(Ala,Glu,Lys,Tyr)6:2:5:1	SIG_53H5516	0.125
119	INSRR	1	150	Poly(Ala,Glu,Lys,Tyr)6:2:5:1	SIG_53H5516	0.25
120	IRAK1	2	10	RB-CTF	13	2
121	IRAK4	6	20	Histone H2B	SIG_87H7445	0.25
122	ITK	1	100	Poly(Glu,Tyr)4:1	SIG_20K5903	0.125
123	JAK2	7	100	Poly(Ala,Glu,Lys,Tyr)6:2:5:1	SIG_53H5516	0.125
124	JAK3	2	200	Poly(Ala,Glu,Lys,Tyr)6:2:5:1	SIG_53H5516	0.125
125	JNK1	5	5	ATF2	6	0.25
126	JNK2	3	5	ATF2	6	0.25
127	JNK3	4	5	ATF2	6	0.25
128	KIT T670I	2	100	Poly(Glu,Tyr)4:1	SIG_20K5903	0.125
129	KIT wt	8	50	Poly(Glu,Tyr)4:1	SIG_20K5903	0.125
130	LCK	3	50	Poly(Glu,Tyr)4:1	SIG_20K5903	0.125
131	LIMK1	1	50	RBER-CHKtide	23	2
132	LTK	1	50	Poly(Glu,Tyr)4:1	SIG_20K5903	0.125
133	LYN	1	20	Poly(Glu,Tyr)4:1	SIG_20K5903	0.125
134	MAP4K4	1	5	Casein	SIG_83K7430	0.5
135	MAPKAPK3	1	20	tetra(LRRWSLG)	4	0.25
136	MAPKAPK5	5	10	RBER-CHKtide	23	4
137	MARK1	1	100	RBER-CHKtide	23	1
138	MARK2	2	4,5	RBER-CHKtide	23	2
139	MARK3	1	100	RBER-CHKtide	17	1
140	MATK	1	5	Poly(Glu,Tyr)4:1	SIG_20K5903	0.125
141	MEK1 wt	2	50	ERK2-KR (kinase-dead)	6	2
142	MELK	1	100	RBER-CHKtide	23	2
143	MERTK	1	50	Poly(Glu,Tyr)4:1	SIG_20K5903	0.5
144	MET	12	25	Poly(Ala,Glu,Lys,Tyr)6:2:5:1	SIG_53H5516	0.125
145	MET T1250M	1	20	Poly(Ala,Glu,Lys,Tyr)6:2:5:1	SIG_53H5516	0.125
146	MINK1	2	10	RBER-CHKtide	24	1

Table W1. (*continued*)

No.	Kinase	Lot	Conc. (ng/50 µl)	Substrate	Lot	Conc. (µg/50 µl)
147	MKK6 S207D/T211D	1	50	p38-alpha-KA (kinase-dead)	1	1
148	MST1	2	5	RB-CTF	13	2
149	MST2	3	10	RB-CTF	13	2
150	MST3	1	20	Casein	SIG_65K7410	1
151	MST4	1	100	RB-CTF	13	1
152	mTOR	1	20	Casein	SIG_65K7410	1
153	MUSK	3	150	Poly(Ala,Glu,Lys,Tyr)6:2:5:1	SIG_53H5516	0.125
154	MYLK2	1	10	S6-peptide	4	1
155	NEK1	1	3	RBER-CHKtide	24	4
156	NEK11	1	25	Myelin Basic Protein	MIL_28053	2
157	NEK2	2	100	RB-CTF	13	1
158	NEK3	1	5	S6-peptide	4	2
159	NEK6	1	20	GSK3(14-27)	7	2
160	NEK7	2	15	Casein	SIG_83K7430	1
161	NIK	3	200	RBER-CHKtide	24	2
162	NLK	2	15	GSK3(14-27)	9	2
163	p38-alpha	5	10	ATF2	6	0.5
164	p38-beta	4	3	ATF2	10	1
165	p38-delta	1	2	RBER-CHKtide	24	2
166	P38-gamma	1	2,5	RB-CTF	13	1
167	PAK1	2	15	tetra(LRRWSLG)	6	1
168	PAK2	1	50	tetra(LRRWSLG)	5	0.25
169	PAK3	1	20	tetra(LRRWSLG)	5	0.5
170	PAK4	3	50	tetra(LRRWSLG)	6	0.5
171	PAK6	1	50	tetra(LRRWSLG)	4	0.125
172	PAK7	1	50	tetra(LRRWSLG)	4	0.25
173	PASK	1	50	RBER-CHKtide	17	2
174	PBK	3	200	Histone H1	SIG_94H8010	0.5
175	PCTAIRE1	4	400	RBER-CHKtide	23	2
176	PDGFR-alpha	9	50	Poly(Ala,Glu,Lys,Tyr)6:2:5:1	SIG_53H5516	0.125
177	PDGFR-beta	13	50	Poly(Ala,Glu,Lys,Tyr)6:2:5:1	SIG_53H5516	0.125
178	PDK1	2	20	tetra(LRRWSLG)	5	0.25
179	PHKG2	1	10	RBER-CHKtide	24	4
180	PIM1	3	10	GSK3(14-27)	8	1
181	PIM2	2	50	GSK3(14-27)	7	2
182	PKA	2	5	tetra(LRRWSLG)	5	0.5
183	PKC-alpha	5	2,5	PKC(19-31)	2	0.25
184	PKC-beta1	4	2,5	PKC(19-31)	2	0.25
185	PKC-beta2	3	5	PKC(19-31)	2	0.25
186	PKC-delta	4	50	PKC(19-31)	2	0.5
187	PKC-epsilon	6	10	PKC(19-31)	2	0.5
188	PKC-eta	5	20	Histone H2B	SIG_87H7445	0.25
189	PKC-gamma	7	10	MEK1-KM (kinase-dead)	2	0.25
190	PKC-iota	6	100	PKC(19-31)	2	0.5
191	PKC-mu	4	12,5	RBER-CHKtide	23	2
192	PKC-nu	2	50	tetra(LRRWSLG)	6	0.125
193	PKC-theta	8	2,5	PKC(19-31)	2	0.25
194	PKC-zeta	5	50	PKC(19-31)	2	0.5
195	PLK1	13	50	RBER-CHKtide	17	2
196	PLK3	1	30	Casein	SIG_65K7410	0.5
197	PRK1	4	25	RBER-CHKtide	23	2
198	PRK2	1	10	RBER-CHKtide	24	4
199	PRKD2	1	3	RBER-CHKtide	24	4
200	PRKG1	1	5	PKC(19-31)	2	1
201	PRKG2	1	1	GSK3(14-27)	6	4
202	PRKX	1	10	GSK3(14-27)	6	4
203	PYK2	1	75	Poly(Glu,Tyr)4:1	SIG_20K5903	0.125
204	RAF1 Y340D/Y341D	1	10	MEK1-KM (kinase-dead)	21	0.5
205	RET	1	20	Poly(Glu,Tyr)4:1	SIG_20K5903	0.125
206	RIPK2	3	50	RBER-CHKtide	24	2
207	ROCK1	2	4	PKC(19-31)	2	1
208	ROCK2	2	2,5	S6-peptide	4	2
209	RON	2	2,5	p38-alpha-KA (kinase-dead)	3	1
210	ROS	1	15	Poly(Ala,Glu,Lys,Tyr)6:2:5:1	SIG_53H5516	0.125
211	RPS6KA1	2	10	RBER-CHKtide	23	2
212	RPS6KA2	1	5	tetra(LRRWSLG)	5	0.5
213	RPS6KA3	2	5	MEK1-KM (kinase-dead)	4	0.25
214	RPS6KA4	1	50	RBER-CHKtide	17	2
215	RPS6KA5	1	25	RBER-CHKtide	17	2
216	RPS6KA6	1	2	GSK3(14-27)	8	2
217	S6K	6	50	GSK3(14-27)	6	4
218	S6K-beta	1	100	RBER-CHKtide	24	4
219	SAK	3	100	p38-alpha-KA (kinase-dead)	4	4

Table W1. (*continued*)

No.	Kinase	Lot	Conc. (ng/50 µl)	Substrate	Lot	Conc. (µg/50 µl)
220	SGK1	4	200	GSK3(14-27)	7	1
221	SGK2	1	20	GSK3(14-27)	6	1
222	SGK3	4	50	GSK3(14-27)	9	1
223	SNARK	1	100	Histone H2B	SIG_87H7445	0.5
224	SNF1LK2	1	2,5	RBER-CHKtide	24	2
225	SNK	5	50	GSK3(14-27)	7	2
226	SRC	4	10	Poly(Glu,Tyr)4:1	SIG_20K5903	0.125
227	SRPK1	1	200	MEK1-KM (kinase-dead)	UPS_DAM1475041	1
228	SRPK2	1	200	Myelin Basic Protein	UPS_DAM1475041	1
229	STK17A	1	25	RB-CTF	13	4
230	STK23	2	25	RBER-CHKtide	24	4
231	STK33	1	50	RBER-CHKtide	24	2
232	SYK	3	100	Poly(Glu,Tyr)4:1	SIG_20K5903	0.125
233	TAOK2	2	10	Casein	SIG_83K7430	1
234	TAOK3	5	50	PKC(19-31)	2	0.5
235	TBK1	2	5	Casein	SIG_65K7410	1
236	TEC	1	200	Poly(Glu,Tyr)4:1	SIG_20K5903	0.125
237	TGFB-R1	3	10	GSK3(14-27)	8	1
238	TIE2	7	10	Poly(Ala,Glu,Lys,Tyr)6:2:5:1	SIG_53H5516	0.125
239	TRK-A	1	50	Poly(Glu,Tyr)4:1	SIG_20K5903	0.125
240	TRK-B	4	10	Poly(Glu,Tyr)4:1	SIG_20K5903	0.25
241	TRK-C	5	10	Poly(Glu,Tyr)4:1	SIG_20K5903	0.125
242	TSF1	2	25	Casein	SIG_65K7410	1
243	TSK2	2	25	RBER-CHKtide	21	2
244	TSSK1	1	3	RBERvCHKtide	24	2
245	TTK	3	100	RBER-CHKtide	23	1
246	TYK2	1	80	Poly(Ala,Glu,Lys,Tyr)6:2:5:1	SIG_53H5516	0.125
247	TYRO3	1	25	Poly(Glu,Tyr)4:1	SIG_20K5903	0.5
248	VEGF-R1	9	50	Poly(Glu,Tyr)4:1	SIG_20K5903	0.125
249	VEGF-R2	15	25	Poly(Glu,Tyr)4:1	SIG_20K5903	0.125
250	VEGF-R3	12	20	Poly(Glu,Tyr)4:1	SIG_20K5903	0.125
251	VRK1	1	50	RBER-CHKtide	21	2
252	WEE1	5	200	Poly(Ala,Glu,Lys,Tyr)6:2:5:1	SIG_53H5516	0.125
253	WNK2	1	30	RBER-CHKtide	24	2
254	WNK3	1	10	S6-peptide	4	2
255	YES	1	20	Poly(Glu,Tyr)4:1	SIG_20K5903	0.125
256	ZAP70	1	20	Poly(Glu,Tyr)4:1	SIG_20K5903	0.125

Table W2. Kinase Residual Activity after Treatment with 100 nM JLK1486.

ABL1 T315I	98
ABL1 wt	92
ABL2	95
ACK1	104
ACV-R1	98
ACV-R1B	97
ACV-RL1	110
AKT1	103
AKT2	107
AKT3	109
ALK	113
AMPK-α1 fl	103
ARK5	99
Aurora-A	96
Aurora-B	102
Aurora-C	106
AXL	104
BLK	96
BMX	98
B-RAF V600E	102
B-RAF wt	90
BRK	106
BRSK1	114
BTK	120
CAMK1D	121
CAMK2A	83
CAMK2B	78
CAMK2D	95
CAMK4	103
CAMKK2	119
CDC42BPA	102
CDC42BPB	95
CDK1/CycA	96
CDK1/CycB1	121
CDK1/CycE	102
CDK2/CycA	92
CDK2/CycE	91
CDK3/CycE	96
CDK4/CycD1	93
CDK4/CycD3	105
CDK5/p25NCK	99
CDK5/p35NCK	90
CDK6/CycD1	88
CDK7/CycH/MAT1	45
CDK8/CycC	69
CDK9/CycT	98
CHK1	110
CHK2	76
CK1-α1	67
CK1-δ	100
CK1-ε	109
CK1-γ1	96
CK1-γ2	105
CK1-γ3	106
CK2-α1	105
CK2-α2	94
CLK1	90
COT	88
CSF1-R	95
CSK	112
DAPK1	177
DAPK2	83
DAPK3	75
DCAMKL2	70
DDR2	76
DMPK	88
DYRK1A	98
EEF2K	106
EGF-R L858R	99
EGF-R T790M	112
EGF-R T790M/L858R	104
EGF-R wt	115
EIF2AK2	99
EIF2AK3	99
EPHA1	108

Table W2. (*continued*)

EPHA2	107
EPHA3	107
EPHA4	108
EPHA5	97
EPHA7	100
EPHA8	118
EPHB1	109
EPHB2	95
EPHB3	96
EPHB4	123
ERBB2	97
ERBB4	97
ERK2	87
FAK fl	104
FER	103
FES	108
FGF-R1	107
FGF-R1 VM	93
FGF-R2	109
FGF-R3	100
FGF-R4	103
FGR	110
FLT3 D835Y	97
FLT3 wt	92
FRK	103
FYN	112
GRK2	107
GRK3	103
GRK4	100
GRK5	98
GRK6	87
GSK3-α	99
GSK3-β	91
HCK	112
HIPK1	88
HIPK3	141
HRI	102
IGF1-R	120
IKK-α	91
IKK-β	104
IKK-ε	103
INS-R	99
INSRR	95
IRAK1	92
IRAK4	111
ITK	107
JAK2	100
JAK3	97
JNK1	114
JNK2	109
JNK3	111
KIT wt	106
LCK	91
LIMK1	94
LTK	114
LYN	101
MAP4K4	90
MAPKAPK3	106
MAPKAPK5	94
MARK1	99
MARK2	89
MARK3	108
MATK	123
MEK1 wt	92
MELK	103
MERTK	102
MET	103
MINK1	105
MKK6 S207D/T211D	91
MST1	115
MST2	95
MST3	93
MST4	108
MUSK	101
MYLK2	99

Table W2. (*continued*)

NEK1	121
NEK11	102
NEK2	102
NEK3	119
NEK6	100
NEK7	111
NIK	93
NLK	106
p38-α	121
p38-β	123
p38-γ	105
PAK1	106
PAK2	103
PAK3	101
PAK4	97
PAK6	113
PAK7	96
PASK	87
PBK	109
PCTAIRE1	108
PDGFR-α	100
PDGFR-β	95
PDK1	105
PHKG2	108
PIM1	104
PIM2	88
PKA	101
PKC-α	102
PKC-β1	104
PKC-β2	81
PKC-δ	82
PKC-ε	114
PKC-η	101
PKC-γ	98
PKC-ι	106
PKC-μ	93
PKC-ν	92
PKC-θ	107
PKC-ζ	101
PLK1	95
PLK3	107
PRK1	104
PRK2	104
PRKD2	123
PRKG1	108
PRKG2	103
PRKX	112
PYK2	111
RAF1 Y340D/Y341D	99
RET	103
RIPK2	108
ROCK1	96
ROCK2	96
RON	98
ROS	100
RPS6KA1	89
RPS6KA2	105
RPS6KA3	108
RPS6KA4	93
RPS6KA5	118
RPS6KA6	99
S6K	105
S6K-β	105
SAK	86
SGK1	109
SGK2	100
SGK3	109
SNARK	96
SNF1LK2	109
SNK	105
SRC	99
SRPK1	97
SRPK2	87
STK17A	78
STK23	106

Table W2. (*continued*)

STK33	107
SYK	99
TAOK2	122
TBK1	99
TEC	104
TGFB-R1	100
TIE2	99
TRK-A	110
TRK-B	102
TRK-C	133
TSF1	97
TSK2	97
TSSK1	91
TTK	104
TYK2	92
TYRO3	116
VEGF-R1	116
VEGF-R2	112
VEGF-R3	99
VRK1	106
WEE1	99
WNK2	109
WNK3	101
YES	114
ZAP70	107

The detailed description of the kinase assay is provided in Table W1 and its legend.
In the current table, a residual activity of 120% means that 100 nM JLK1486 increases by 20% the kinase activity compared to the control.

Table W3. Virtual Screening of Three Isoforms with Vina Software.

	Compounds*		
PPAR Isoform	JLK1486	Rosiglitazone	Troglitazone
α	−8.60	−8.30	−10.00
δ	−11.90	−9.00	−10.10
γ	−10.00	−9.10	−9.80

*Each result is the mean of the best result of five independent docking experiments, in kilocalories per mole as obtained with the Vina scoring function.